ACS APPLIED MATERIALS & INTERFACES
Research Article
www.acsami.org

Electric Field-Induced, Reversible Lotus-to-Rose Transition in Nanohybrid Shish Kebab Paper with Hierarchical Roughness

Eric D. Laird,[†] Ranjita K. Bose,[‡] Hao Qi,[†] Kenneth K. S. Lau,*[,‡] and Christopher Y. Li*[,†]

[†]Department of Materials Science and Engineering, and [‡]Department of Chemical and Biological Engineering, Drexel University, 3141 Chestnut Street, Philadelphia, Pennsylvania 19104, United States

Supporting Information

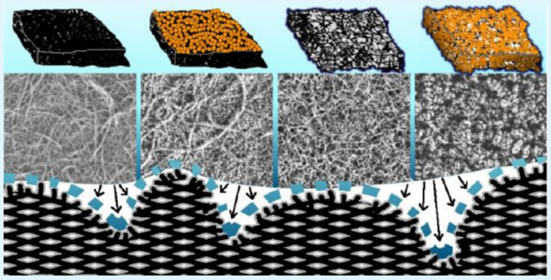

ABSTRACT: Nature uses a variety of strategies to tune wetting behavior for biological applications. By artificially mimicking these strategies, a variety of different wetting conditions can be achieved. Numerous examples exist of designed surfaces that can mimic the wetting behavior of lotus leaves or rose petals, but few surfaces that may reversibly transition between the two have been reported. In this paper, a combination of topological control over conductive, carbon-based nanomaterials and low surface energy coating was used to tune the wetting properties between "lotus" and "rose." The topological control was imparted by a hierarchical "nanohybrid shish kebab" structure, which uses solution-grown polymer single crystals on carbon nanotubes to tune the surface roughness of the latter. The low surface energy polytetrafluoroethylene (PTFE) coating was deposited by the initiated chemical vapor deposition technique. Application of electric potential on these unique nanostructures allows the surfaces to reversibly transition between "lotus" and "rose" behavior. A further irreversible transition between "rose" and the fully wetted Wenzel wetting state was also predicted and shown. These materials show remarkable promise for lab-on-a-chip devices and surface passivation for biological studies.

KEYWORDS: *superhydrophobic surface, hierarchical structure, polymer wetting, carbon nanotubes, polymer crystallization, nanohybrid shish kebab*

INTRODUCTION

The term "superhydrophobicity" is generally defined as having water contact angles greater than 150°.[1,2] The superhydrophobic lotus leaf[1] is an archetypical example of this nonwetting behavior, which is termed the "Cassie–Baxter condition" (or sometimes the "lotus effect"). Profound wetting states with superhydrophobicity have been reported, and the nomenclature in this field is loosely defined.[1,3−12] In general though, the surface must have a high enough pore aspect ratio to be able to support air pockets beneath the droplet to help lift the droplet over the surface. Most superhydrophobic surfaces show high contact angle, low contact angle hysteresis, and low water surface adhesion.[2,11] However, considerable adhesive forces can also exist between droplet and surface depending on the pore geometry and surface chemistry. This has led to other seemingly contradictory terms such as "sticky superhydrophobicity,"[13−15] wherein a surface maintains a high contact angle but is able to pin a water drop, even to suspend the drop upside down. The nonwetting but still highly adhesive red rose petal is a naturally occurring example of another mechanism for this behavior and so lends its name to what has been termed the "petal effect". In this case, nature uses dual-length scale roughness which prevents droplet penetration into submicroscale features, but allows wetting to occur into microscale depressions.[14−16]

A material that can reversibly transition between robust lotus and rose states could be tremendously useful for microfluidics applications, biomedical applications, self-cleaning surfaces, liquid optics, surface-catalyzed electrolysis, and lab-on-a-chip devices.[17] However, fabrication of such a surface is challenging. Dawood et al. showed how a single silicon substrate could be used to template both "petal" and "lotus" effects, but this behavior was spatially selective and fixed.[18] A few groups have attempted to use azobenzene derivatives[19] or diarylethene coatings[20−22] on a range of geometries to achieve phototunable superhydrophobic adhesive surfaces. Early work in this direction was irreversible[21] or the versatility was limited between several relatively adhesive states.[19] Through careful manipulations of diarylethene coatings, Uchida and co-workers were able to demonstrate reversible "lotus" to "rose" wetting behaviors, although complete melting and precisely controlled isomer recrystallization over a 30 h period was required.[22]

Another promising approach to control wetting behavior is electrowetting, which involves applications of electrical potential across a liquid/dielectric/electrode capacitor, which can lead to a charge-induced imbalance of forces near the liquid/dielectric contact line, and a resultant decrease in the

Received: September 10, 2013
Accepted: October 28, 2013
Published: October 28, 2013

dx.doi.org/10.1021/am403925f | *ACS Appl. Mater. Interfaces* 2013, 5, 12089−12098

Scheme 1. SWCNTs (Enlarged Schematic Shown in the Top Left Corner) Dispersed in Solution[a]

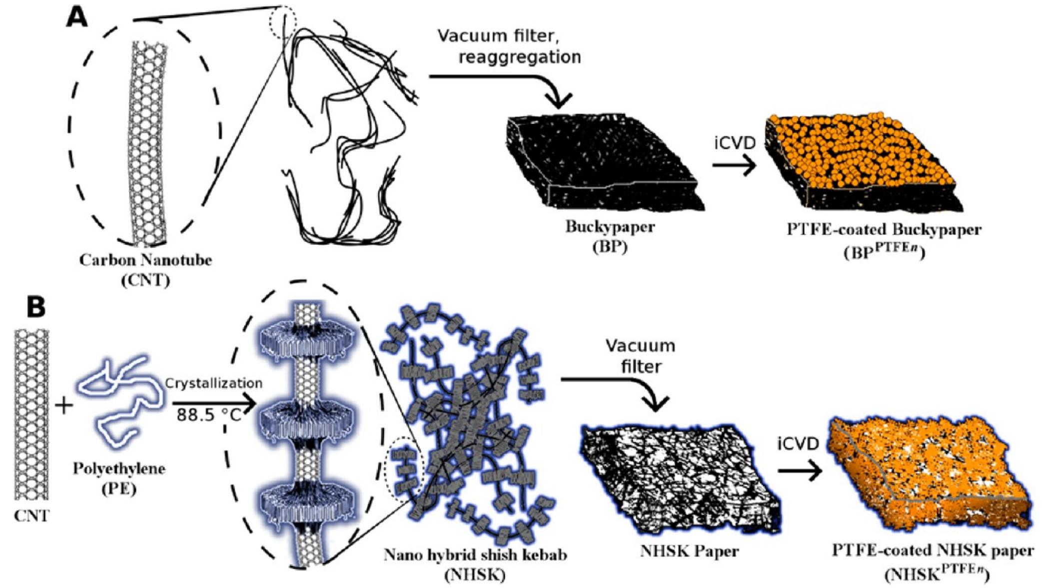

[a] Following pathway **A**, vacuum deposition can be used to form SWCNT buckypaper, although reaggregation of SWCNT in solution can also occur. On the other hand, PE single crystals can be solution-grown on CNT sidewalls to produce a robust physical functionalization (pathway **B**). Through a similar vacuum-filtration step, a PE single crystal-decorated buckypaper analog called "NHSK paper" can be produced. iCVD decoration of SWCNT buckypaper and NHSK paper forms BP^{PTFEn} and $NHSK^{PTFEn}$ films.

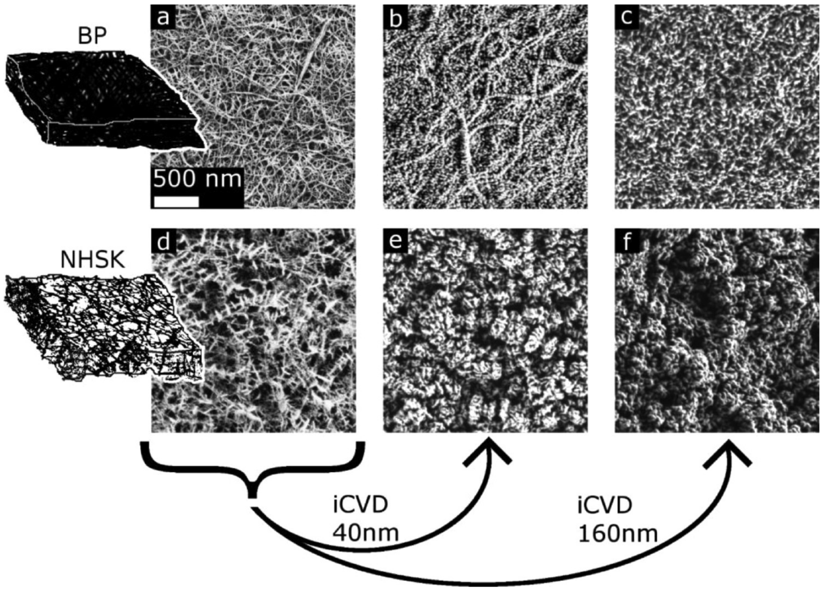

Figure 1. SEM micrographs showing the morphologies of pristine surfaces and iCVD PTFE coatings on carbon-based nanomaterials. (a) SWCNT buckypaper. (b and c) SWCNT buckypaper coated with 40 and 160 nm equivalent coating thickness of PTFE, respectively, as would be expected if deposited on a bare silicon wafer. (d) NHSK paper. (e and f) NHSK paper coated with equivalent of 40 (e) and 160 nm (f) PTFE coatings.

observed contact angle. Kakade et al. showed an electrowetting-induced superhydrophobic to superhydrophilic transition over multiwalled carbon nanotube (MWCNT) buckypapers.[23] Verplank et al. used electrowetting to transition between Cassie and Wenzel states and were able to do so reversibly using silicon nanowires coated with short-chain fluorocarbon.[24] To introduce reversible electrowetting, it is generally necessary to involve some extrinsic stimuli, such as substrate heating or the addition of oil to replace the ambient phase.[17] To date, to the best of our knowledge, no material exists that shows a direct, fast, reversible transition from a "lotus leaf" to a "rose petal" (abbreviated as "lotus to rose").

In our previous work, we showed how solution grown polymer single crystals nucleated from single walled carbon nanotube (SWCNT) sidewalls, "nanohybrid shish kebabs" (NHSK),[25−27] could be vacuum-filtered to form a conductive paper with controllable porosity (Scheme 1).[28] It was shown that the controllable porosity and the "programed" addition of low-surface energy polyethylene (PE) crystallites could be used to directly control the wettability. This NHSK paper showed rose petal behavior, allowing droplets up to 5 μL to be suspended upside down despite having contact angles above 152°. Herein, we report that polytetrafluoroethylene (PTFE) coatings could be used to tune the hydrophobicity of NHSK paper using initiated chemical vapor deposition (iCVD), a solvent-free surface polymerization technique.[29] The resultant hierarchical structure shows complex, yet tunable wetting states, including micro-Cassie−nano-Cassie (Cassie^{m}−Cassie^{n}, the lotus state), micro-Wenzel−nano-Cassie (Wenzel^{m}−Cassie^{n}, the rose petal state), and micro-Wenzel−nano-Wenzel (Wenzel^{m}−Wenzel^{n}). Furthermore, using electrowetting, 10 μL droplets were able to be reversibly suspended upside down, while droplets as large as 50 μL could be pinned to the extent that they could be manipulated easily. This lotus-to-rose transition was fully reversible (i.e., gently teasing the droplet could unpin it from the surface). Wetting was found to be irreversible if voltages were sufficiently high to transition from rose to the fully wetted Wenzel state.

RESULTS AND DISCUSSION

Structure and Morphology of iCVD Functionalized CNT Surfaces with Hierarchical Roughness. Two carbon nanomaterial-based substrates are the focus of the present study: SWCNT buckypaper and NHSK paper were decorated with PTFE using the iCVD technique (Scheme 1, detailed procedure in the Methods section and Supporting Information). Figure 1a and d show the SEM micrographs of these surfaces. Salient properties of these substrates are as follows. SWCNT buckypaper as formed by vacuum deposition without the aid of surfactant is a dense material made up of bundles of 1 nm CNTs, where the mean bundle diameter is ~13 nm (although a large range exists, with some individualized tubes and few-tube bundles, and some bundles on the order of 100 nm). Over a 0.5 × 0.7 mm surface region, the root-mean-square roughness (R_{RMS}) was found to be 497 nm. NHSK paper as shown in Figure 1d is an analog of SWCNT buckypaper with controllable roughness which is imparted by polymer single crystals (PSCs).[28] The PSC lamellae are oriented perpendicularly/oblique to the CNT axes and the surface of the NHSK paper. The sizes of the PSCs dictate the pore size and the nanoscale roughness—and consequently influence the conductivity and wetting properties. The pore size and surface properties of NHSK paper can be selected by adjusting the feeding concentration of polymer used in NHSK formation. In films with a polymer content of 75 wt %, the single crystal diameter averages 48 nm, the average "intrakebab spacing" (defined as the width of the gallery between adjacent lamellae) is 55 nm. Unlike the dense surface of SWCNT buckypaper, however, the surface of NHSK paper is dominated by voids, which form an interpenetrating, porous network throughout the interior of the material. Figure 1b, c, e, and f show the appearances of each surface after PTFE coating. BET surface area analysis of NHSK paper (Figure 1d) showed a broad distribution of mesopores,[28] whereas SWCNT paper (Figure 1a) is comprised largely of micropores ~2 nm and some mesopores of around 4−6 nm between bundles of CNTs.[30,31]

The iCVD technique has been shown to be effective in forming conformal polymer coatings on complicated 3D structures,[32,33] curved surfaces,[34] and can even conformally coat high aspect ratio pores[35] and CNT forests.[36−38] Nevertheless, the limits of this technique would be tested in attempting to coat the interior of the above-mentioned porous films, which are approximately 15 μm in depth, along pores with variable diameter that follow tortuous path. Because iCVD is an adsorption limited process, it should be noted that the physical differences between the pore size distributions of these substrates can be expected to influence the filling percentage of those pores.[39,40] Pore filling requires the transport of gas phase monomer which is dominated by Knudsen diffusion: it is hypothesized that a window of partial pressures exists wherein the time constant for monomer diffusing within the porous material is shorter than that of the surface reaction rate.[40] This had an effect on the amount of polymer deposited as will be shown later, but did not impact the specific results of this study.

The morphologies of these films after iCVD coating at different thicknesses are shown in Figure 1. Figure 1b and c shows the morphology of PTFE grown on SWCNT buckypaper, designated BP$^{\mathrm{PTFE}n}$, where n is either 40 or 160, indicating the equivalent coating thickness (nm) on a silicon wafer. PTFE crystallites grown in situ showed a clear NHSK-type morphology after shorter deposition times (BP$^{\mathrm{PTFE40}}$), i.e. PTFE formed single crystals that are strung together periodically by SWCNTs.[29] These "relief NHSK" manifested in a quasi-two-dimensional (2D) arrangement with PTFE lamellae oriented normal to the SWCNT bundle axes. This structure seemed to closely mimic the top surface of NHSK paper shown in Figure 1d (albeit with lower apparent microscale roughness), an important point that will be revisited later. The structure observed was similar to previous observations of PTFE recrystallized after mechanical deformation, although in the present case no external influence was applied.[41] Longer deposition times resulted in overgrowth and impingement of the crystallites (Figure 1c), which produced a disorganized top surface with apparently less influence from the underlying relief topology. PTFE deposited on NHSK paper led to remarkable PTFE crystallites on the top surface (Figure 1e and f). This organization was maintained at both short (NHSK$^{\mathrm{PTFE40}}$, Figure 1e) and long (NHSK$^{\mathrm{PTFE160}}$, Figure 1f) deposition times, although the structure was much more clearly defined in the former case. Longer depositions showed a transition toward a spherulitic structure. Both of these samples demonstrated high aspect ratio asperities at both the micro and nano length scales.

Figure 2 depicts energy dispersive X-ray spectroscopy (EDS) maps of cross sections of the SWCNT buckypaper film and the NHSK paper. Fluorine maps are shown as blue dots in Figure 2b and d. For comparison purposes, the map of carbon intensity is shown in the Supporting Information (Figure S.3) to confirm the absence of low-intensity "dead regions". Figure 2e suggests that the SWCNT buckypaper shows almost no signal from fluorine atoms below the top surface of the film. There, the fluorine signal is extremely strong but it comes primarily from a flap of material that partially delaminated from the buckypaper film. The fluorine intensity within the buckypaper film is weak and intermittent, although some fluorine-enriched veins are evident. In contrast, the fluorine content of the NHSK paper gradually tapers to a minimum at a depth of 11.5 μm, but is never exhausted. Having a conformal coating throughout the depth of the material is critical to the applications, because it allows the material's dynamic wetting behavior to show full reversibility as will be explained in detail below.

The qualitative results above are in agreement with the quantitative data taken from XPS depth profiling. Due to the prohibitively long times required to sputter through the sample, it was difficult to recover the fluorine profile through the entire depth of the films, but comparative results can be drawn by examining the fluorine/carbon atomic ratio r for a depth profile

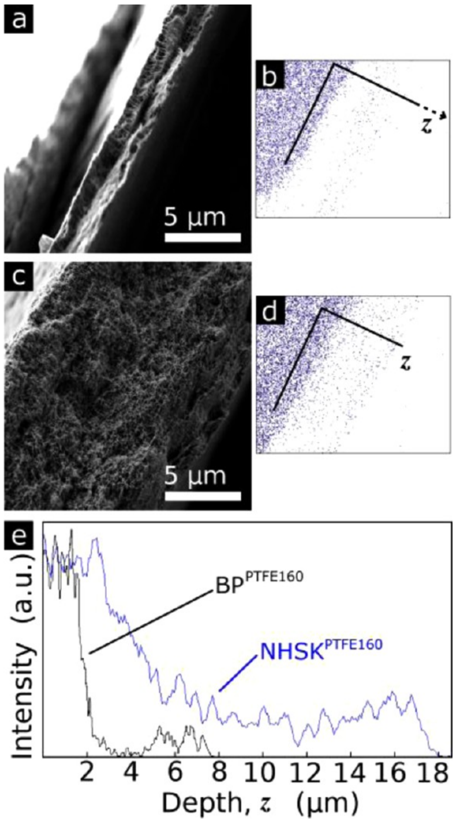

Figure 2. Electron micrographs of cross sections and EDS maps of fluorine from same within BP^{PTFE160} (a and b) and NHSK^{PTFE160}samples (c and d). (e) Average intensity profiles of cross sections of BP^{PTFE160} and NHSK^{PTFE160} as a function of depth (normalizd by fluorine intensity at top surfaces).

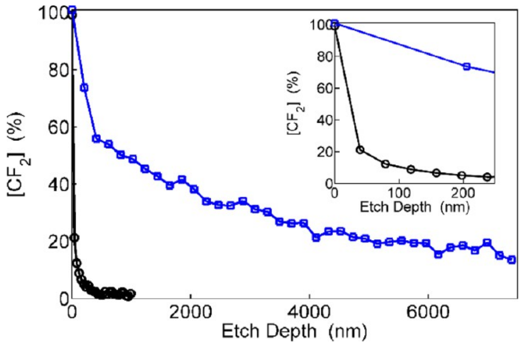

Figure 3. [CF$_2$] vs etch depth (equivalent coating thickness of 160 nm) for two of the substrates examined in this study: circles BP^{PTFE160}; squares NHSK^{PTFE160}. (inset) Detail of the first several minutes of sputtering depth profiling (total of 5 min for NHSK^{PTFE160}, 9 min for BP^{PTFE160}).

for the ablated region (Figure 3). It should be noted that argon sputtering of PTFE has been shown to alter the chemistry of PTFE films, but has a negligible effect on the actual atomic concentration.[42] The ratio r can therefore be used to determine the relative concentrations of CF$_2$ and nonfluorine-bound carbons by mol %. By monitoring the atomic concentration, the percentage of material that is "shelved" CF$_2$ as opposed to nonfluorine-bound carbon can be determined as $[CF_2] = 3r/(2 + 2r)$ (derivation in the Supporting Information). Comparing this ratio with the EDS results can be done by measuring the thickness of the ablated film ex situ to determine the etch depth. BP^{PTFE160} was sputtered for a total of 24 min and ablated approximately 950 nm of material (just under 40 nm/min). The NHSK^{PTFE160} sample was sputtered for 180 min, which ablated an estimated 7.4 μm of the material (~41 nm/min).

The results from EDS mapping and XPS depth profiling satisfy a conceptual picture of these two different substrates as barriers to monomer infiltration. SWCNT buckypaper shows a [CF$_2$] depth profile with some fluorine content in the interior of the film, but the CF$_2$ groups are heavily enriched at the surface. Because the SWCNTs are subject to reaggregation into disorganized bundles of varying size, a few pathways that can be infiltrated by monomer are left open. On the other hand, NHSK paper forms a poor barrier against gas phase initiator monomer molecules, thus allowing an eventual PTFE coating that conforms to the surface throughout the depth of the spongelike, nanostructured material. This is consistent with the observations of the surface morphological development as described above and shown in Figure 1.

Wetting Properties of PTFE-Coated Buckypaper and NHSK Paper. Wetting behaviors of the various carbon substrates have been systematically studied as shown in Figure 4. SWCNT buckypaper used in this study, like graphite, is slightly hydrophilic and has a contact angle of 82.2 ± 1.9° (Figure 4a). NHSK papers formed from SWCNT with PE shish kebabs can demonstrate a range of sessile drop contact angles. By varying the size of the PE shish kebab (for instance, by changing the polymer/CNT feeding ratio), contact angles can

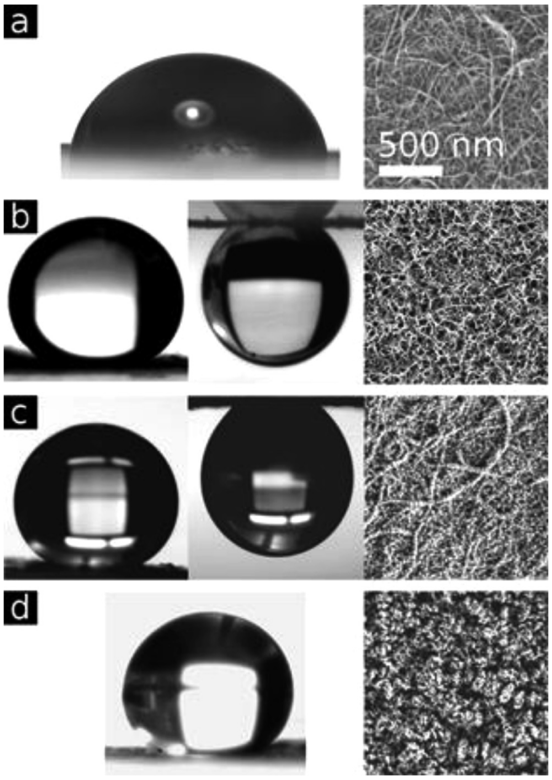

Figure 4. Wetting properties of buckypaper and NHSK paper films. (a) Sessile drop on SWCNT buckypaper. (b) NHSK paper, showing the "sticky superhydrophobicity" effect and the ability to suspend a 5 μL droplet upside down. (C) BP^{PTFE40} paper, showing some similar droplet wetting/adhesion effects shown in part b. (d) NHSK^{PTFE40} film with a 5 μL droplet deposited on the surface. The droplet was mobile and formed a nonwetting "Cassie" state on the surface.

be tuned from ~116° to well over 150°, which marks the superhydrophobic condition (Figure 4b). Dynamic wetting behavior is also strongly influenced by the surface topology. Specifically, droplet pinning was observed for the superhydrophobic films made using a PE:CNT ratio of 3:1. The static contact angle was found to be 152.3°, while advancing and receding contact angles for these films were found to be 166.6° and 93.7°, respectively, indicating strong adhesion despite the high contact angle. Droplets up to 5 μL could be suspended upside down without roll-off. The reason for this is the hierarchical roughness of the film, which is due to inter- and intraNHSK (see Scheme 2a). The quasi-periodic arrangement of the kebab crystals contributes to the nanoscale roughness while the 2D random packing of these NHSKs leads to an inter-NHSK, microscale roughness that is ~619 nm obtained by image analysis. Water can wet the microscale features while, at the nanoscale, asperities are formed between polymer lamellae that are inaccessible to the droplet. Accordingly, this dual-length scale wetting property is called a Wenzel$^{\mathrm{m}}$–Cassie$^{\mathrm{n}}$ (denotes microscale-Wenzel–nanoscale-Cassie) state. The contact angle can be predicted as

Scheme 2. Wetting Behavior of NHSK Films without (a) and with (c) PTFE Coating and SWCNT Buckypaper with PTFE Coating (b)[a]

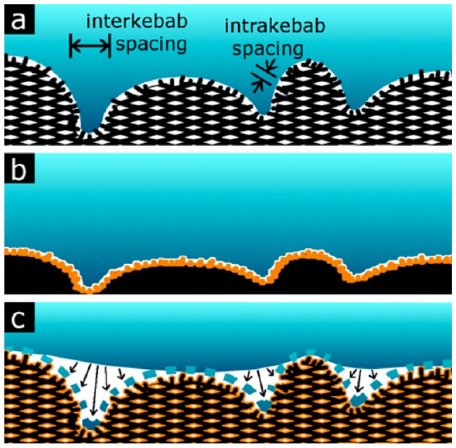

[a] Parts a and b represent the petal effect. Microscale features (interkebab regions) are wetted by the droplet whereas the nanoscale features (intrakebab regions) remain inaccessible to the water drop. In part c, the droplet is excluded from both the micro- and nanoscale features, representative of the lotus effect. Microscale asperities can be wetted with an external influence such as an electric field or vibration, causing a reversible transition to the petal effect.

$$\cos\theta = f_{\mathrm{n}}(r_{\mathrm{m}}\cos\theta^{\mathrm{Y}} + 1) - 1 \tag{1}$$

Here, θ^{Y} is the Young contact angle for a smooth surface, θ is the observed contact angle, r_{m} is the microscale roughness, and f_{n} is the wetted fraction at the nanoscale for a surface with a Cassie–Baxter wetting condition.

To understand why the droplet cannot initially wet the nanoscale regions, it is important to consider the Young–Laplace pressure (P_{YL}) required to deform the droplet to wet the intrakebab gallery. This pressure is dependent on the radius of curvature as shown in refs 43 and 44. This equation can be simplified along the principal radii of curvature of the droplet.[6] The Young–Laplace pressure for a droplet at maximum distention into a shish kebab gallery can be written as

$$P_{\mathrm{YL}} = \gamma^{\mathrm{LV}}\left(\frac{2}{D} + \frac{2}{d_{\mathrm{intra}}}\right) \tag{2}$$

where γ^{LV} is the liquid–vapor surface energy (72.8 mN m^{-1} for the water/air interface), D is the kebab diameter, and d_{intra} is the intrakebab distance, i.e. the width of the gallery between adjacent shish kebabs. For a pristine NHSK paper with a 3:1 PE:CNT ratio, the diameter of the polymer single crystal averages 54.8 nm in diameter, and the intrakebab gallery spacing averages 57.2 nm. The Young–Laplace pressure required to deform a water droplet into such an asperity is 5.2 MN m^{-2}. Significant external influence would be required to overcome this barrier for droplet deformation. Thus, the droplet is excluded from the intrakebab gallery. On the other hand, NHSKs are vacuum-filtered haphazardly, creating microscale furrows in the paper surface. These "interkebab" regions have a relatively shallow aspect ratio, with depths on the order of tens of nanometers and widths on the order of hundreds of nanometers or even micrometers. Therefore, the radius of curvature of a droplet sitting above these furrows is relatively large. For an interkebab region of 0.5 μm^2 and a depth of 50 nm, the Young–Laplace pressure required to deform a droplet to wet the interkebab region is much smaller, estimated to be on the order of 29 kN m^{-2}, requiring significantly less external influence to overcome. Consequently, spreading a droplet over the surface creates adhesion between the NHSK paper surface and the droplet as the latter settles into the microscale furrows.

On the basis of the above analysis, it was expected that this "statically superhydrophobic but dynamically non-sliding" behavior would also be observed on buckypaper surfaces decorated with PTFE kebabs through the iCVD technique (see Figure 4c). As shown in Figure 1, PTFE shish kebabs on the BP$^{\mathrm{PTFE40}}$ surface are smaller and closer together, with a kebab diameter of ~40 nm and an intrakebab spacing of 13 nm. PTFE is an ultralow surface energy solid. CF$_2$ groups have surface energy γ = 23 mN m^{-1}; CF$_3$ groups have γ = 15 mN m^{-1};[45,46] the combined surface energy for this polymer is generally cited[47,48] as being between 18 and 21 mN m^{-1} but is also dependent on molecular weight[45] and crystallinity.[49,50] Because PTFE is more hydrophobic than PE (intrinsic contact angle of ~115°), the water droplet must be raised at the nanoscale, but the furrows are shallower than those of PE so the droplet is able to wet the surface on the microscale. Again, statically superhydrophobic but dynamically nonsliding behavior is observed. The sample surface has a higher static contact angle (158°) and can even suspend a larger drop size than NHSK paper (5.5 μL). The adhesive force required to suspend such a droplet is 54.0 μN, which is about 10% higher than that shown by NHSK paper.

NHSK paper coated with PTFE demonstrates a different behavior. These surfaces do not pin sessile drops. This is true of each of the PTFE-coated NHSK films. The advancing/receding contact angles of NHSK$^{\mathrm{PTFE40}}$ are 169.9°/166.2° (Figure 4d). The adhesive force for this surface is calculated to be much lower: roughly 0.86 μN for a 5 μL droplet. This indicates that droplets on the surface of NHSK$^{\mathrm{PTFE40}}$ are in a Cassie–Baxter state on both micro- and nanoscales. Droplet body forces are virtually identical to those required to deform the droplet enough to wet the pristine NHSK film's furrows; coating the sample with PTFE lifts the droplet higher off of the NHSK film, shifting the wetting state from the Wenzel$^{\mathrm{m}}$–Cassie$^{\mathrm{n}}$ condition to a Cassie$^{\mathrm{m}}$–Cassie$^{\mathrm{n}}$ condition.

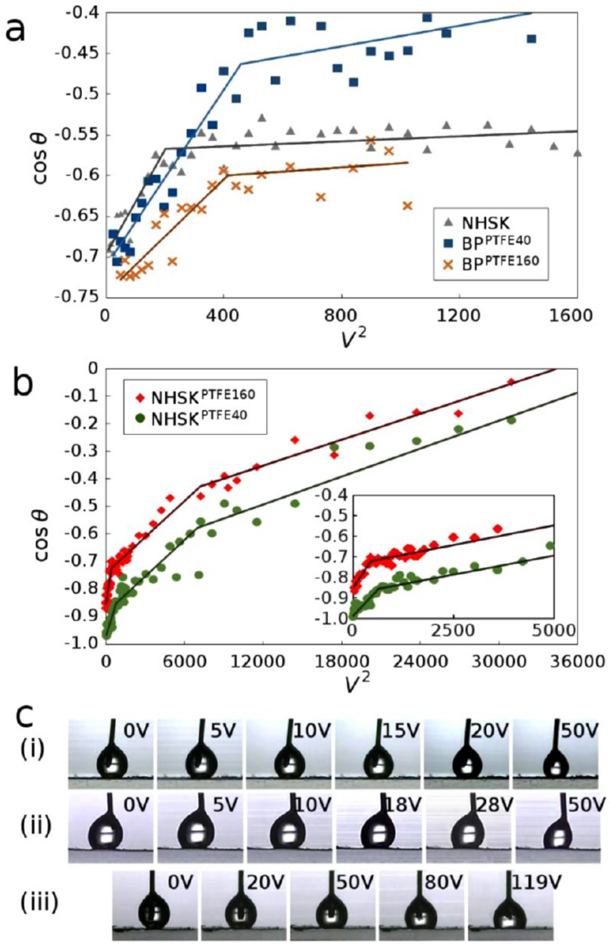

Figure 5. Electrowetting of NHSK, BP$^{\mathrm{PTFE}}$, and NHSK$^{\mathrm{PTFE}}$ films. (a) cos(θ) versus V^2 for electrowetting of 10 μL droplets on NHSK, BP$^{\mathrm{PTFE40}}$, and BP$^{\mathrm{PTFE160}}$ samples. (b) Same as part a for NHSK$^{\mathrm{PTFE40}}$ and NHSK$^{\mathrm{PTFE160}}$ samples. (c) Wetting evolution of 10 μL droplets on (i) NHSK, (ii) BP$^{\mathrm{PTFE40}}$, and (iii) NHSK$^{\mathrm{PTFE160}}$ films at voltages shown, stepped +1 V after every 20 s.

Electrowetting Properties of PTFE-Coated Buckypaper and NHSK Paper. With the exception of pristine buckypaper, each of these films has a conductive scaffold with a dielectric buffer layer supporting the drop above the conductive region. Thus, they are ideal candidates for using electrowetting as a means to tune the wetting states. At constant compression and chemical potential, the Lippmann equation describes the effect of applied potential V on interfacial tension as $\partial\gamma^{\mathrm{SL}}/\partial V = -q$, where q is the charge density.[51] Taking the derivative of the Lippmann equation with respect to V and combining it with Young's equation leads to

$$\cos\theta_V = \cos\theta^{\mathrm{Y}} + \frac{CV^2}{2\gamma^{\mathrm{LV}}} \tag{3}$$

where θ_V is the apparent contact angle at applied voltage V, and C is the capacitance per unit area. Torkelli noted[52] that polarization of the droplet occurs at the solid surface, and thus eq 3 does not correctly describe electrowetting behavior in the Cassie state. In this case, the Cassie–Baxter equation must be modified to reflect that the droplet is supported by the solid fraction:

$$\cos\theta_V = f(\cos\theta^{\mathrm{Y}} + 1) + \frac{fCV^2}{2\gamma^{\mathrm{LV}}} - 1 \tag{4}$$

In the Wenzel$^{\mathrm{m}}$–Cassie$^{\mathrm{n}}$ wetting state, the Wenzel microscale roughness must also be accounted for. The resulting equation for contact angle in this state under the influence of an applied voltage ($\theta_V^{\mathrm{Wm-Cn}}$) takes the following form:

$$\cos\theta_V^{\mathrm{Wm-Cn}} = \frac{f_{\mathrm{n}}CV^2}{2\gamma^{\mathrm{LV}}} + f_{\mathrm{n}}(r_{\mathrm{m}}\cos\theta^{\mathrm{Y}} + 1) - 1 \tag{5}$$

Electrostatic pressure (P_{elec}) is given as

$$P_{\mathrm{elec}} = \frac{\varepsilon_0 E^2}{2} = \frac{2\varepsilon_0 V^2}{D^2} \tag{6}$$

where ε_0 is the permittivity of free space and E is the magnitude of the electric field. If $P_{\mathrm{elec}} > P_{\mathrm{YL}}$, the droplet will be drawn to overcome the corresponding roughness.[53] In the present case, since we have two levels of roughness, two Young–Laplace pressures can be defined, i.e. $P_{\mathrm{YL}}^{\mathrm{m}}$ and$P_{\mathrm{YL}}^{\mathrm{n}}$. The mathematic expression of the three possible wetting states at different voltages can be summarized as follows:

$$\cos\theta_V = \begin{cases} \dfrac{fC_1V^2}{2\gamma^{\mathrm{LV}}} + f(\cos\theta^{\mathrm{Y}} + 1) - 1 & \dfrac{F_{\mathrm{B}}}{A} + \dfrac{2\varepsilon_0V^2}{D^2} < P_{\mathrm{YL}}^{\mathrm{m}} \quad \text{case 1} \\ \dfrac{f_{\mathrm{n}}C_2V^2}{2\gamma^{\mathrm{LV}}} + f_{\mathrm{n}}(r_{\mathrm{m}}\cos\theta^{\mathrm{Y}} + 1) - 1 & \dfrac{F_{\mathrm{B}}}{A} + \dfrac{2\varepsilon_0V^2}{D^2} > P_{\mathrm{YL}}^{\mathrm{m}} \cup \dfrac{2\varepsilon_0V^2}{D^2} < P_{\mathrm{YL}}^{\mathrm{n}} \quad \text{case 2} \\ \dfrac{C_3V^2}{2\gamma^{\mathrm{LV}}} + r\cos\theta^{\mathrm{Y}} + 1 & \dfrac{2\varepsilon_0V^2}{D^2} > P_{\mathrm{YL}}^{\mathrm{n}} \quad \text{case 3} \end{cases} \tag{7}$$

Here, r is the Wenzel roughness, A is the geometric area of contact between the droplet and the film, and F_{B} is the body force of the droplet. The subscripts for the capacitances 1, 2, and 3 correspond to the three different possible wetting cases, Cassie$^{\mathrm{n}}$–Cassie$^{\mathrm{m}}$, Wenzel$^{\mathrm{m}}$–Cassie$^{\mathrm{n}}$, and Wenzel$^{\mathrm{m}}$–Wenzel$^{\mathrm{n}}$, respectively. Equation 7 suggests that increasing voltage can transition wetting states from case 1 to 2 to 3. By plotting cos θ_V vs V^2, it is also possible to find best fits of f_{n} as well as the capacitance. More interestingly, the threshold voltages V^{T12} for the transition from Cassie$^{\mathrm{n}}$–Cassie$^{\mathrm{m}}$ to Wenzel$^{\mathrm{m}}$–Cassie$^{\mathrm{n}}$, as well as the transition from Wenzel$^{\mathrm{m}}$–Cassie$^{\mathrm{n}}$ to Wenzel$^{\mathrm{m}}$–Wenzel$^{\mathrm{n}}$ wetting behavior, V^{T23}, can be easily obtained as the points where the slope of the plot changes. Specifically, it can be anticipated that there should be a threshold voltage that can provide the electric field strength required to wet the intrakebab gallery. This transition should be unambiguous: the applied potential needed to draw the droplet into the gallery is well in excess of the potential for hydrolysis, so

Table 1. Properties of SWCNT and NHSK-Based Films and Physical Constants Determined by Electrowetting[a]

	BP^{PTFE40}	$BP^{PTFE160}$	NHSK	$NHSK^{PTFE40}$	$NHSK^{PTFE160}$
D (nm)/Δ_D^*	43.1/1.29	93.9/1.73	54.8/1.60	52.6/1.44	52.0/1.42
d_{intra} (nm)/ Δ_d^*	13.0/1.92	18.3/1.70	57.2/1.52	27.6/1.46	44.0/1.39
θ^0 (deg)	158.0	154.2	152.3	169.3	157.7
θ_A/θ_R (deg)	165.5/93.4	162.7/89.1	166.6/93.7	169.9/166.2	163.3/157.0
V_{obs}^{T12} (V)				21	23
θ^{T12} (deg)				150.5	136.9
C_1 (F/m^2)				4.18×10^{-4}	2.04×10^{-4}
f				5.3%	21.7%
V_{obs}^{T23} (V)	19	19	13	90	90
θ^{T23} (deg)	117.4	126.9	124.3	126.6	115.8
C_2 (F/m^2)	1.29×10^{-4}	1.04×10^{-4}	2.80×10^{-5}	1.39×10^{-5}	2.81×10^{-4}
f_n	39.3%	40.8%	33.1%	20.7%	42.4%

[a] Diameter of lozenge-shaped crystal (D) and "intrakebab" distance (d_{intra}) and their multiplicative standard deviations (Δ_D^* and Δ_d^*, respectively) determined from log-normal distribution fitting; initial static contact angle (θ^0, measured independently); advancing and receeding contact angles (θ_R and θ_A, also measured independently); the observed transition voltage (V_{obs}^{T12}) and corresponding contact angle (θ^{T12}) for the case 1 to case 2 transition; capacitance per unit area (C_1) and wetted fraction (f) of films in the Cassie–Baxter state; observed transition voltages for the case 2 to case 3 transition (V_{obs}^{T23}) and the corresponding contact angle (θ^{T23}); the capacitance per unit area (C_2) and wetted fraction (f_n) of the films in the adhesive state, case 2.

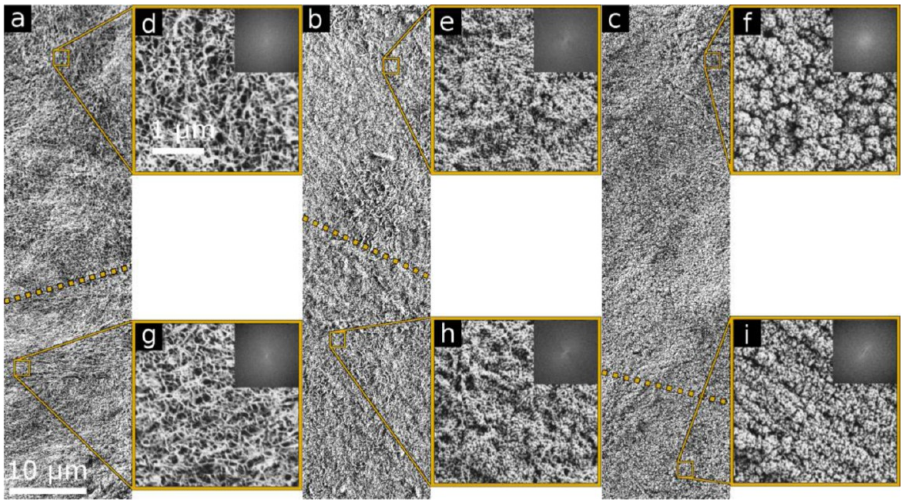

Figure 6. Appearances of films after electrowetting to case 3. (a) NHSK, (b) BP^{PTFE40}, and (c) $NHSK^{PTFE160}$ electrowetted to maximum voltages indicated in Figure 5b. Dotted line boundaries in a–c indicate the leading edge of the droplet after reaching the Wenzel wetting regime. (d–f) Undistorted regions of (d) NHSK, (e) BP^{PTFE40}, and (f) $NHSK^{PTFE160}$ after electrowetting experiment. (d–f inset) Fast Fourier transforms (FFTs) of each surface, showing general lack of orientation. (g–i) Detail of surfaces distorted by the droplet leading edge after transitioning from case 2 ($Wenzel^m$–$Cassie^n$) to case 3 (Wenzel). FFTs of surfaces shown as insets in d–i, suggesting shear alignment in g–i. Surfaces wetted only to case 1 or case 2 did not show any change in orientation after wetting.

bubbles should be observed immediately after the transition occurs. Hydrolysis would be expected to prevent the advance of the contact line: therefore electrowetting should reach a limiting contact angle and show unstable behavior due to bubble generation.

Figure 5 shows the experimental verification of the multistep wetting hypothesis described above (Figure 5a and b) and the electrowetting development of model cases (i) NHSK, (ii) BP^{PTFE40}, and (iii) $NHSK^{PTFE160}$ (Figure 5c). Table 1 lists the characteristics of the films based on fitting using eq 7. Figure 5a shows that NHSK and BP^{PTFEn} samples start with rose petal effect behavior as shown in Figure 4b and c, and these samples are adhesive throughout this range. For such surfaces, increasing voltage leads to a transition from case 2 to case 3, and the observed voltages V_{obs}^{T23} are 19, 19, and 13 V for BP^{PTFE40}, $BP^{PTFE160}$, and NHSK, respectively (Table 1). Using image analysis, we can obtain quantitative information about D and d_{intra}, and then, predict V_{calc}^{T23} by comparing P_{elec} and P_{YL}. Taking NHSK and BP^{PTFE40} as examples,[28,29] the predicted values of V_{calc}^{T23} are 36.6 and 29.7 V for BP^{PTFE40} and NHSK, respectively, which are higher than the observed voltages. Since the $Wenzel^n$ to $Cassie^n$ transitions depend on Young–Laplace curvature, wider intrakebab spacings or smaller kebab diameters allow this transition to occur at lower voltages. The discrepancy can therefore be attributed to the breadths of the distributions.[54]

For the lotus surfaces (initially at case 1, i.e. $NHSK^{PTFE40}$ and $NHSK^{PTFE160}$), two transitions were observed as shown in Figure 5b, corresponding to a transition from lotus to rose and rose to Wenzel, respectively. It is intriguing that within the rose region, gently perturbing the droplet with a pipet allows the droplet to become unstuck and recover its extremely low sliding angle, suggesting that the lotus-to-rose transition is reversible. Figure 5c shows contact angle decreases with increasing voltage below the case 2−case 3 transition, and in each case, above this transition, the contact angle remains fairly stable but the volume decreases due to electrolysis. At elevated voltages, the initially superhydrophobic films become increasingly adhesive toward water. Above 60 V, it was observed that $\mathrm{NHSK^{PTFE160}}$ could pin a 10 μL droplet to at least 45° angle of inclination after the electrode was removed. To confirm that the behavior observed was not due to oxidation by dielectric breakdown,[55] current−voltage experiments were performed in a Faraday cage using a fresh sample. Dielectric breakdown was observed suddenly above 109 V, but below that voltage, the current remained close to zero. Details of this experiment appear in the Supporting Information.

The slopes in Figure 5a and b provide a unique means to calculate capacitance per area. As shown in Table 1. The calculated values of the capacitance per area for $\mathrm{NHSK}^{\mathrm{PTFE}n}$ samples are highest in case 1 and are reduced by an order of magnitude after the transition to case 2. $\mathrm{BP}^{\mathrm{PTFE}n}$ and NHSK samples had roughly the same capacitance per unit area in case 2 as the $\mathrm{NHSK}^{\mathrm{PTFE}n}$ samples had in case 1. This can be explained as double layer charges are increasingly more difficult to build up as the pore size decreases (from microroughness to nanoroughness). When geometric area was factored in, all samples were observed to have capacitance values in the hundreds of picofarad to nanofarad range. Presumably, if $\mathrm{NHSK}^{\mathrm{PTFE}n}$ samples could be made to be the ground wetting state in case 2, the capacitance should be higher before the transition to the Wenzel state.

Figure 6 shows the surfaces of NHSK, $\mathrm{BP^{PTFE40}}$, and $\mathrm{NHSK^{PTFE160}}$ after eletrowetting experiments for 20 s at 40, 50, and 200 V, respectively (each having gone beyond $V_{\mathrm{obs}}^{\mathrm{T23}}$ and the onset of hydrolysis). The surfaces appear slightly distorted at the droplet edge, pulled along the direction of surface tension. This effect is difficult to observe at low magnifications, but at high magnification, the shear alignment of the surface material is apparent. This behavior is consistent with previous observations about the importance of the three-phase contact line.[56,57] Post-Wenzel morphological changes are specific to the surface. On NHSK paper (Figure 6a, d, and g), the NHSK directed into regular striations, suggesting that the charge transfer is efficient across the surface above the case 2−case 3 transition. The $\mathrm{BP^{PTFE40}}$ surface changes are minimal (Figure 6b, e, and h), as the subsurface SWCNT are prevented from participating due to the relatively planar PTFE coating. In Figure 6c, the $\mathrm{NHSK^{PTFE160}}$ surface after electrowetting is shown. The difference between the undeformed surface (Figure 6f) and the surface transformed by the case2−case3 transition (Figure 6i) is relatively dramatic, although these changes are exclusively orientational and much higher voltages are required. This explains why even larger droplets can be suspended from the $\mathrm{NHSK^{PTFE160}}$ surface after electrowetting at high voltages than can be pinned by pristine NHSK films. The lotus-to-rose electrowetting transition is fully reversible between 30 and 90 V, but after overcoming the conditions needed for the transition from rose-to-Wenzel, water drawn into the surface allows the shish kebabs to be reoriented by the extreme conditions created by electrolysis of the droplet.

■ CONCLUSION

Conductive SWCNT based films with hierarchical roughness, i.e. SWCNT buckypaper and NHSK paper, were fabricated by combining controlled solution crystallization, solution filtration and iCVD. NHSK paper has an open, porous structure, thus the iCVD process was able to conformally coat the interior of the film. SWCNT buckypaper, on the other hand, formed an effective barrier against gas-phase monomer infiltration. The resulting films had unique morphological characteristics and properties. SWCNT buckypaper templated PTFE single crystals in situ, a quasi-2D "relief" analog of bare NHSK paper was obtained. NHSK paper substrates caused the PTFE to crystallize in lamellar rings over the kebabs. The resulting morphologies showed markedly different wetting behavior that was attributed to the hierarchical roughness. Reversible lotus-to-rose electrowetting transitions of droplets were observed over NHSK papers coated in PTFE—this phenomenon may have important implications for biointerfacing and microfluidics.

■ METHODS

NHSK Paper Fabrication. SWCNT were purchased from Unidym and processed into buckypaper as described in previous work[28] (this method is also described in the Supporting Information). The method for producing NHSK was described previously;[25−27,58−62] details are also provided in the Supporting Information. These materials were arranged on silicon wafers using kapton tape for PTFE deposition in an iCVD reactor. Hexafluoropropylene oxide (HFPO) and the initiator perfluoro-1-butanesulfonyl fluoride (PBSF) were used as received from Aldrich and had purity of at least 99%.

iCVD Polymerization of PTFE. PTFE depositions were carried out in a custom-made stainless steel vacuum reactor. HFPO and PBSF were metered into the reactor using a mass flow controller (MKS Instruments) and a precision needle valve (Swagelok). Flow rates for PBSF and HFPO were 5 and 20 sccm, respectively. The backside-cooled stage was maintained at 20 °C, and the tungsten filament array was heated to 300 °C. A downstream throttle valve and a pressure controller from MKS Instruments were connected to a dry vacuum pump from Edwards Vacuum to maintain pressure at 300 mTorr. These conditions were chosen to obtain what would be expected to be conformal coatings of 40 and 160 nm over silicon wafers. After coating, the samples were left under vacuum for an additional 20 min to allow quenching of free radicals. These coatings were expected to have significant variance of coating thickness on the SWCNT-based substrates, given the relatively rough topology of the substrate and propensity for individual polymer crystal templating. An interferometry system was used in situ to monitor the deposition rate over regions of planar silicon. This system used a 633 nm HeNe laser from JDS Uniphase passing through a glass window positioned on top of the reactor.

Structural Characterization and Electrowetting. All SEM microscopy was performed on a Zeiss Supra 50VP in high vacuum mode. Samples were sputtered from an 80/20 Pt/Pd target using a Cressington sputter coater prior to imaging. Top surfaces were imaged at 1 kV; fracture surfaces used 2 kV. The same instrument running at 5 kV was used for generating elemental maps using energy dispersive X-ray spectroscopy (EDS). A modular Oxford Instruments Energy Dispersive X-ray Microanalyzer was used for this experiment. Profilometry was used to measure the microscale surface roughness, using a Zygo NewView 6000 optical profiler with 0.1 nm height resolution and 15 000 μm range. Samples were scanned over 0.5 mm × 0.7 mm regions, and 10 linescans of 0.1 mm were analyzed to estimate the surface roughness properties. X-ray photoelectron spectroscopy (XPS) depth profiling was performed using a Physical Electronics Versaprobe 5000 with an Al Kα anode and a 100 μm diameter beam spot. Between scans, the sample was sputtered with argon at 1 kV, 2 μA. Electrowetting was performed on a custom-built contact angle setup using optical elements from Thorlabs. A platinum wire was used as the counter electrode. The buckypaper and NHSK films were cleaved and the edge was painted with silver paint to form the working electrode contact and connected to the negative terminal of the power supply. Applied voltage was monitored with a digital multimeter. Each electrowetting data point represents the average of four measurements (sessile drop measurements were taken as an average of 8−10 measurements). A Keithley model 6450 picoammeter was used for current measurements.

■ ASSOCIATED CONTENT

Supporting Information

Detailed experimental procedures and compositional analysis of the sample. This material is available free of charge via the Internet at http://pubs.acs.org.

■ AUTHOR INFORMATION

Corresponding Authors

*E-mail: chrisli@drexel.edu.
*E-mail: klau@drexel.edu.

Notes

The authors declare no competing financial interest.

■ ACKNOWLEDGMENTS

This work was supported by the National Science Foundation grant DMR-1308958.

■ REFERENCES

(1) Feng, X. J.; Jiang, L. *Adv. Mater.* **2006**, *18*, 3063−3078.

(2) Roach, P.; Shirtcliffe, N. J.; Newton, M. I. *Soft Matter* **2008**, *4*, 224−240.

(3) Gao, L.; McCarthy, T. J. *Langmuir* **2008**, *24*, 9183−9188.

(4) Wenzel, R. N. *Ind. Eng. Chem.* **1936**, *28*, 988−994.

(5) Bico, J.; Thiele, U.; Quéré, D. *Coll. Surf., A* **2002**, *206*, 41−46.

(6) de Gennes, P. G.; Brochard-Wyart, F.; Quere, D. *Capillarity and Wetting Phenomena: Drops, Bubbles, Pearls, Waves*; Springer, 2004.

(7) Liu, G.; Fu, L.; Rode, A. V.; Craig, V. S. J. *Langmuir* **2011**, *27*, 2595−2600.

(8) Bormashenko, E. *Langmuir* **2011**, *27*, 12769−12770.

(9) Liu, G.; Rode, A.; Fu, L.; Craig, V. S. J. *Langmuir* **2011**, *27*, 13962−13963.

(10) Anantharaju, N.; Panchagnula, M. V.; Vedantam, S.; Neti, S.; Tatic-Lucic, S. *Langmuir* **2007**, *23*, 11673−11676.

(11) Cassie, A. B. D.; Baxter, S. *Trans. Faraday Soc.* **1944**, *40*, 546−551.

(12) Deng, X.; Mammen, L.; Butt, H. J.; Vollmer, D. *Science* **2012**, *335*, 67−70.

(13) Guo, Z. G.; Liu, W. M. *Appl. Phys. Lett.* **2007**, *90*, 223111−3.

(14) Bhushan, B.; Nosonovsky, M. *Philos. Trans. R. Soc., A* **2010**, *368*, 4713−4728.

(15) Feng, L.; Zhang, Y.; Xi, J.; Zhu, Y.; Wang, N.; Xia, F.; Jiang, L. *Langmuir* **2008**, *24*, 4114−4119.

(16) Jeong, H. E.; Lee, S. H.; Kim, J. K.; Suh, K. Y. *Langmuir* **2006**, *22*, 1640−1645.

(17) Heikenfeld, J.; Dhindsa, M. *J. Adhes. Sci. Technol.* **2008**, *22*, 319−334.

(18) Dawood, M. K.; Zheng, H.; Liew, T. H.; Leong, K. C.; Foo, Y. L.; Rajagopalan, R.; Khan, S. A.; Choi, W. K. *Langmuir* **2011**, *27*, 4126−4133.

(19) Li, C.; Cheng, F.; Lv, J. A.; Zhao, Y.; Liu, M.; Jiang, L.; Yu, Y. *Soft Matter* **2012**, *8*, 3730−3733.

(20) Kitagawa, D.; Kobatake, S. *Chem. Sci.* **2012**, *3*, 1445−1449.

(21) Uchida, K.; Nishikawa, N.; Izumi, N.; Yamazoe, S.; Mayama, H.; Kojima, Y.; Yokojima, S.; Nakamura, S.; Tsujii, K.; Irie, M. *Angew. Chem., Int. Ed.* **2010**, *49*, 5942−5944.

(22) Nishikawa, N.; Uyama, A.; Kamitanaka, T.; Mayama, H.; Kojima, Y.; Yokojima, S.; Nakamura, S.; Tsujii, K.; Uchida, K. *Chem.−Asian J.* **2011**, *6*, 2400−2406.

(23) Kakade, B.; Mehta, R.; Durge, A.; Kulkarni, S.; Pillai, V. *Nano Lett.* **2008**, *8*, 2693−2696.

(24) Verplanck, N.; Galopin, E.; Camart, J. C.; Thomy, V.; Coffinier, Y.; Boukherroub, R. *Nano Lett.* **2007**, *7*, 813−817.

(25) Laird, E. D.; Li, C. Y. *Macromolecules* **2013**, *46*, 2877−2891.

(26) Li, C. Y.; Li, L.; Cai, W.; Kodjie, S. L.; Tenneti, K. K. *Adv. Mater.* **2005**, *17*, 1198−1202.

(27) Li, L.; Li, B.; Hood, M. A.; Li, C. Y. *Polymer* **2009**, *50*, 953−965.

(28) Laird, E. D.; Wang, W.; Cheng, S.; Li, B.; Presser, V.; Dyatkin, B.; Gogotsi, Y.; Li, C. Y. *ACS Nano* **2012**, *6*, 1204−1213.

(29) Laird, E. D.; Bose, R. K.; Wang, W.; Lau, K. K. S.; Li, C. Y. *Macromol. Rapid Commun.* **2013**, *34*, 251−256.

(30) Sun, C. H.; Li, F.; Cheng, H. M.; Lu, G. Q. *Appl. Phys. Lett.* **2005**, *87*, 243109−3.

(31) Zhou, C.; Kumar, S.; Doyle, C. D.; Tour, J. M. *Chem. Mater.* **2005**, *17*, 1997−2002.

(32) Ma, M. L.; Gupta, M.; Li, Z.; Zhai, L.; Gleason, K. K.; Cohen, R. E.; Rubner, M. F.; Rutledge, G. C. *Adv. Mater.* **2007**, *19*, 255−259.

(33) Ma, M. L.; Mao, Y.; Gupta, M.; Gleason, K. K.; Rutledge, G. C. *Macromolecules* **2005**, *38*, 9742−9748.

(34) Lau, K. K. S.; Gleason, K. K. *Adv. Mater.* **2006**, *18*, 1972−1977.

(35) Gupta, M.; Kapur, V.; Pinkerton, N. M.; Gleason, K. K. *Chem. Mater.* **2008**, *20*, 1646−1651.

(36) Lau, K. K. S.; Bico, J.; Teo, K. B. K.; Chhowalla, M.; Amaratunga, G. A. J.; Milne, W. I.; McKinley, G. H.; Gleason, K. K. *Nano Lett.* **2003**, *3*, 1701−1705.

(37) Ozaydin Ince, G.; Demirel, G.; Gleason, K. K.; Demirel, M. C. *Soft Matter* **2010**, *6*, 1635−1639.

(38) Ye, Y.; Mao, Y.; Wang, F.; Lu, H.; Qu, L.; Dai, L. *J. Mater. Chem.* **2011**, *21*, 837−842.

(39) Asatekin, A.; Gleason, K. K. *Nano Lett.* **2010**, *11*, 677−686.

(40) Nejati, S.; Lau, K. K. S. *Nano Lett.* **2010**, *11*, 419−423.

(41) Yang, J.; Williams, R.; Peterson, K.; Geil, P. H.; Long, T. C.; Xu, P. *Polymer* **2005**, *46*, 8723−8733.

(42) Nobuta, T.; Ogawa, T. *J. Mater. Sci.* **2009**, *44*, 1800−1812.

(43) Young, T. *Phil. Trans. R. Soc. London* **1805**, *95*, 65−87.

(44) Laplace, P.-S., *Traité De Mécanique Céleste, Œuvres Complète*; Gauthier-Villars: Paris, 1806; Vol. *4*, s.2.

(45) Dettre, R. H.; Johnson, R. E., Jr. *J. Colloid Interface Sci.* **1969**, *31*, 568−569.

(46) Tsibouklis, J.; Nevell, T. G. *Adv. Mater.* **2003**, *15*, 647−650.

(47) Zisman, W. A. Relation of the Equilibrium Contact Angle to Liquid and Solid Constitution. In *Contact Angle, Wettability, and Adhesion*; American Chemical Society: Washington, D.C., 1964; Vol. *43*, pp 1−51.

(48) Burnham, N. A.; Dominguez, D. D.; Mowery, R. L.; Colton, R. J. *Phys. Rev. Lett.* **1990**, *64*, 1931−1934.

(49) Dettre, R. H.; Johnson, R. E., Jr. *J. Colloid Interface Sci.* **1966**, *21*, 367−377.

(50) Glennon, D.; Cox, P. A.; Nevell, R. T.; Nevell, T. G.; Smith, J. R.; Tsibouklis, J.; Ewen, R. J. *J. Mater. Sci.* **1998**, *33*, 3511−3517.

(51) Bockris, J. O. M.; Reddy, A. K. N.; Gamboa-Aldeco, M. E., *Modern Electrochemistry 2a: Fundamentals of Electrodics*; Springer, 2001.

(52) Torkkeli, A. *Droplet Microfluidics on a Planar Surface*; Helsinki University of Technology, Espoo, Finland, 2003.

(53) Dai, W.; Zhao, Y.-P. *J. Adhes. Sci. Technol.* **2008**, *22*, 217−229.

(54) Both intrakebab spacings and kebab diameters follow log-normal statistics. One might consider the intrakebab spacing d_{intra} required for $V_{\mathrm{obs}}^{\mathrm{T23}}$ as a function of kebab diameter D. For $\mathrm{BP}^{\mathrm{PTFE40}}$ samples, $V_{\mathrm{obs}}^{\mathrm{T23}}$ corresponds a statistical maximum at 1.30 standard deviations below the mean for D and 1.29 standard deviations above the mean for d_{intra}. This represents a 1% probability, which is a fairly large population given the difference in length scale. As the voltage is further increased, the probability threshold decreases further.

(55) Papathanasiou, A. G.; Papaioannou, A. T.; Boudouvis, A. G. *J. Appl. Phys.* **2008**, *103*, 034901−4.

(56) Bormashenko, E.; Pogreb, R.; Whyman, G.; Erlich, M. *Langmuir* **2007**, *23*, 6501−6503.

(57) Whyman, G.; Bormashenko, E.; Stein, T. *Chem. Phys. Lett.* **2008**, *450*, 355−359.

(58) Li, L.; Li, C. Y.; Ni, C. Y. *J. Am. Chem. Soc.* **2006**, *128*, 1692−1699.

(59) Li, L.; Wang, W.; Laird, E. D.; Li, C. Y.; Defaux, M.; Ivanov, D. A. *Polymer* **2011**, *52*, 3633−3638.

(60) Li, L. Y.; Li, B.; Yang, G. L.; Li, C. Y. *Langmuir* **2007**, *23*, 8522−8525.

(61) Li, L.; Yang, Y.; Yang, G.; Chen, X.; Hsiao, B. S.; Chu, B.; Spanier, J. E.; Li, C. Y. *Nano Lett.* **2006**, *6*, 1007−1012.

(62) Li, B.; Li, L. Y.; Wang, B. B.; Li, C. Y. *Nat. Nanotechnol.* **2009**, *4*, 358−362.